# Experimental and numerical study of the micro-mechanical failure in composites

**Ashouri Vajari, Danial; Martyniuk, Karolina; Sørensen, Bent F.; Legarth, Brian Nyvang**

*Published in:*
Proceedings of the 19th International Conference on Composite Materials

*Publication date:*
2013

*Document Version*
Publisher's PDF, also known as Version of record

# EXPERIMENTAL AND NUMERICAL STUDIES OF THE MICRO-MECHANICAL FAILURE IN COMPOSITES

D. A. Vajari[1*], K. Martyniuk[2], B. F. Sørensen[2], B. N. Legarth[1]

[1] Department of Mechanical Engineering, Solid Mechanics, Technical University of Denmark, 2800 Kgs. Lyngby, Denmark,
[2] Department of Wind Energy, Section of Composites and Materials Mechanics, Technical University of Denmark, Risø Campus, 4000 Roskilde, Denmark
[*] Corresponding author (dvaj@mek.dtu.dk)

**Abstract**

The fibre/matrix interfacial debonding is found to be the first microscale failure mechanism leading to subsequent macroscale transverse cracks in composite materials under tensile load. In this paper, the micromechanical interface failure in fiber-reinforced composites is studied experimentally and by numerical modeling by means of the finite element analysis. Two fibers embedded in the matrix are subjected to a remote transverse tensile load (see Fig. 1a). The trapezoidal cohesive zone model proposed by Tvergaard and Hutchinson [14] is used to model the fracture of the fiber-matrix interfaces. This study is based on the comparison between the results of numerical modeling and those corresponding to the experimental tests by employing two parameters: The angle from the load direction to the crack tip and the crack normal opening. This comparison aims to investigate the interfacial properties and also assess the progressive fiber-matrix debonding by focusing on the interaction of two fibers with dissimilar interfacial strengths.

## 1 Introduction

Depending on the material properties and loading conditions, interface debonding, matrix failure and/or fiber breakage are the main failure mechanisms in composites. In many cases, interfacial debonding is the first mechanisms which leads to crack initiation and propagation. Therefore, it is important to investigate the interface parameters accurately. The interface fracture energy, $\phi$, and the maximum cohesive stress, $\sigma_{max}$, are the most critical parameters playing significant roles in failure of interfaces. The experimental part of the present research aims at determining the interface parameters. Furthermore, the effects of fiber dimension and fiber spacing on the damage evolution in glass-epoxy composites are studied by means of the numerical simulation. Therefore, as the first step it is necessary to find out a proper experimental test method in order to measure the interface fracture energy and the maximum cohesive stress. The lack of a standard two-dimensional test and its corresponding device is the first problem in selecting the method of experimental test. Different methods have been used to characterize the fiber/matrix interface parameters such as the fragmentation test, the pull-out test, the push-in test and the push-out test. Each of these methods has some advantages and disadvantages which should be

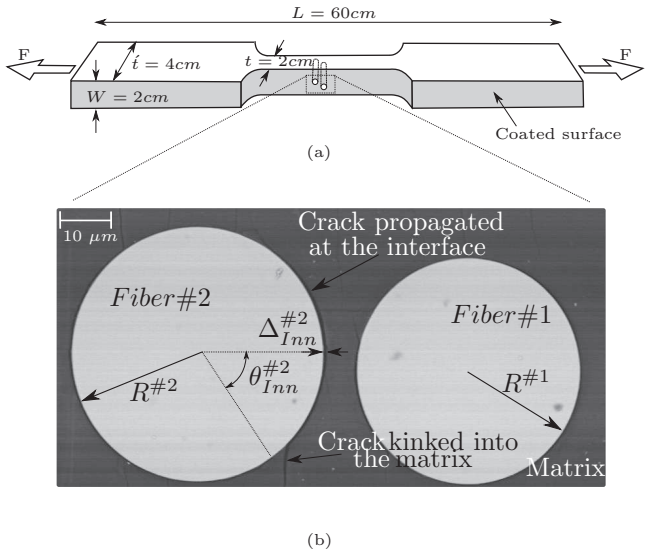


Figure 1: a) Schematic drawing of specimen with a dog-bone shaped epoxy resin including two glass fibers in the middel of specimen. b) Example of debonding obseved in SEM under tensile test.

considered for a specific purpose under investigation. The fragmentation test was proposed by Kelly and Tyson[5] to study the interface properties in metal matrix composites. This method was appropriate for composites with ductile matrices and brittle fibers. While, the pull-out test is usually performed for the tough fibers surrounded by brittle matrix. Although the fragmentation test as well as the pull-out test lead to durable results but their testing conditions can be difficult to fulfill. In the push-in technique a single fiber is pushed by means of a nanoindentor on a cross-section of a bulk specimen of the laminate until interface decohesion occurs. On the other hand, the push-in test does not require any laborious sample preparation. However, the interpretation of this method is somehow difficult because the length of the debonded interface below the surface is not known. Thus, the results should be analyzed in terms of a shear lag model or FE simulations of the test [8]. The push-out test is very similar to the push-in test but is carried out on a very thin specimen. Although the push-out test requires more difficult specimen preparation, but leads to a more direct measurement of the interface strength [2]. However, both the push-in as well as push-out methods involve frictional sliding while the friction law or shear stress is unknown. Thus it is difficult to separate debonding and frictional sliding which happen simultaneously. Furthermore, all above interface measuring techniques try to investigate the tangential properties of the interface. While for the cases subjected to a tensile load normal to the fiber orientation, like the preset study, the dominant debonding is due to normal opening of the interfaces. Thus, in this research another method has been used which approaches to a more direct measurement of the normal properties of fiber/matrix interfaces in uni-directional composites. In this method, a specimen including a single or double fibers embedded in the matrix is subjected to tensile load inside the chamber of the Scanning Electron Microscope (SEM). The cross-section normal to the fiber orientation will be monitored while the load is being applied. By this technique, more precise data with respect to the normal properties of interface such as the cohesive maximum normal stress and cohesive fracture energy can be determined.

This paper comprises five sections. After the introduction the proposed experimental method is presented in detail in the next section. Then, the numerical methods used in the simulation is given in section 3. In the fourth section, the results are shown and discussed. Finally, this study is concluded in section 5.

## 2 Experimental Study

The fiber/matrix interface properties of fiber-reinforced composites are determined according to the transverse tensile test inside the SEM. The glass-fibers used in this experimental study are provided by Ahlstorm. The diameters of fibers are $\sim$ 45-55 $\mu m$. The fibers with large diameter are chosen to measure the interface debonding since this is easier by the SEM. The experimental samples are manufactured by positioning two glass-fibers in a rubber mold. Then, the mold is filled up with a fast-curing epoxy resin named *RIMR 135* (from Momentive company) which surrounds the fibers. The fibers Young's modulus and Poisson's ratio are $E_f = 72GPa$ and $\nu_f = 0.21$, respectively and for the matrix the properties are $E_m = 3GPa$ and $\nu_m = 0.3$. The yield stress of the matrix material is $\sigma_y = 16MPa$. To find the yield stress of the matrix, a parameter study is carried out to fit the numerical debonding angle-remote stress curve as well as the numerical crack normal opening-remote stress cuve with those corresponding to the experimental data. Thermal compressive residual stresses in the fiber along the longitudinal axis as well as in the radial direction arise due to the thermal expansion mismatch between constituent phases, chemical shrinkage of the resin and non-uniform curing [6]. Radial residual stresses in glass fibers embedded in epoxy resin have rather significant contribution to the general process-induced stress state [16]. However, the residual stresses in the longitudinal direction along the fibers are significantly influencing the stresses in the fibers surrounded by a large volume of resin. It has been shown by single-fiber fragmentation tests that fibers without any pre-loading while curing are under compressive residual stresses [16].

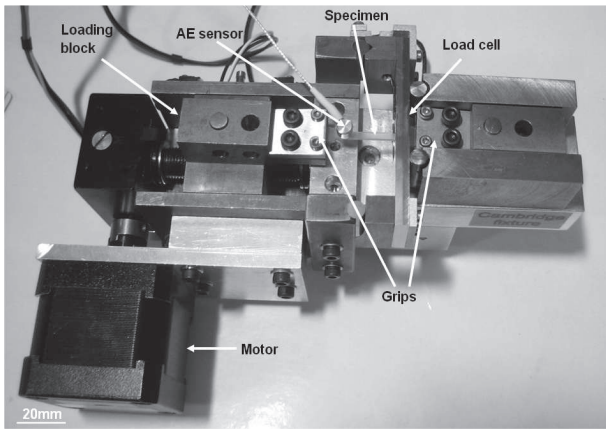


Figure 2: Test set-up for tensile testing in SEM. A motor drives a spindle that moves one of the loading blocks and thus one grip, resulting in tension or compression of the specimen.

Residual stresses could also influence interface properties and cause debonding prior to loading which would prevent studying of interface properties. Therefore, the fibers are pre-loaded before curing. The amount of pre-load can be estimated by calculating the expected compressive residual thermal stress in the fiber. Residual compressive stress of the fibers due to the thermal expansion mismatch between constituent phases are given by [3] and [4]

$$\sigma_f^{th} = (\alpha_m - \alpha_f)(T - T_{ref})\frac{E_f}{1 + (\frac{V_f}{V_m})(\frac{E_f}{E_m})} \quad (1)$$

where, $\alpha_m$ and $\alpha_f$ stands for the thermal expansion coefficient of the matrix and the fibers, respectively. The room temperature is denoted by $T$ and $T_{ref}$ is the reference temperature at which the material solidifies upon cooling. The fiber volume fraction is $V_f$ while the matrix volume fraction is $V_m$. Finally, $E_m$ and $E_f$ denote the Young's modulus of the matrix and the fibers, respectively. The value of the aforementioned parameters are given in Table. 1. During post-curing the samples including two fibers embedded in a large volume of resin are heated at $60°C$. In this temperature the fibers are under a thermal compressive stress of $\sigma_f^{th} = -130MPa$ which corresponds to a strain level of $\varepsilon^{th} = -0.18\%$. However, the above calculation of residual stresses does not include the chemical reactions. Therefore, during manufacturing process the fibers were pre-strained a little more, i.e. $+0.25\%$. This pre-straining fulfills by applying a weight of $20g$ at each fibers ends. After positioning and pre-straining, the mold is filled up with previously degassed resin. Specimen was cured at $23°C$ for 24 hours and subsequently post-curing at $60°C$ for 10 hours. The surface of interest was polished in order to remove any cracks from the surfaces as well as fulfilling microscopy requirements. Once smooth surface is obtained, samples are reshaped to the dog-bone shape in order to facilitate mechanical testing. The final geometry of the sample is shown in Fig. 1a. Then, the surface faced to the microscope is electrically conducted by a thin coating of a carbon layer.

| Material properties | Value |
|---|---|
| $\alpha_m\ [\frac{1}{°C}]$ | $65 \times 10^{-6}$ |
| $\alpha_f\ [\frac{1}{°C}]$ | $5.1 \times 10^{-6}$ |
| $T\ [°C]$ | 20 |
| $T_{ref}\ [°C]$ | 50 |
| $\frac{V_f}{V_m}\ [-]$ | $\approx 0$ (for two-fiber composite) |

Table 1: The thermal parameters of the epoxy resin used for the residual compressive stress calculation.

As shown in Fig. 2, the specimen is subjected to the tensile load using a special tensile loading fixture [11] designed for testing in SEM. The fixture was mounted on the $x, y, z$ stage of the vacuum chamber of SEM (Zeiss, EVO60). The polished surface was oriented towards the microscope electron gun and detectors. By this setting in situ observation of crack initiation under the tensile loading can be obtained. During the micro scale experiments, the load was applied to the specimen in increments. The tensile test was interrupted at various load steps until ultimate failure. This enabled observing and capturing of images of the crack propagation using SEM facilities. The fiber/matrix debonding as well as matrix failure near the fibers is shown in Fig. 1b where a crack is seen to initiate at the interfaces between the fibers and the matrix. It propagates along the fiber/matrix interface until a certain angle is reached, at which the crack kinked into the matrix. This study considers the failure be-

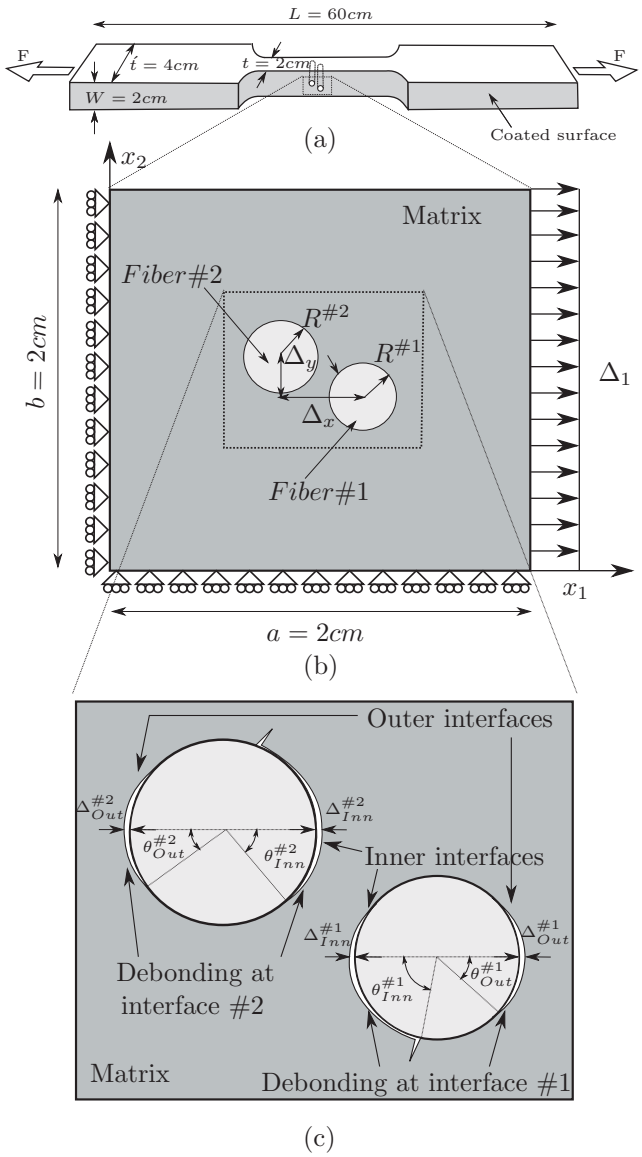


Figure 3: a) Schematic drawing of specimen with a dog-done shaped epoxy resin including two glass fibers in the middle of specimen. b) The chosen 2D-cell from the middle of specimen including two circular fibers. The dimensions, loads and the coordinate system are shown. c) A deformed and partly debonded cell under an $x_1$-direction tensile load.

fore interfacial crack kinks to the matrix. In the results section, it will be shown that the interface at which debonding initiates depends on the strength of the interfaces as well as the size of the fibers.

## 3 Numerical Modeling

To simulate the observed fiber/matrix debonding, two circular fibers are embedded in a large zone of matrix (see Fig. 3b). A Cartesian reference coordinate system, $x_i$, is placed at the bottom-left corner of the cell and aligned with the unit cell edges. The dimension of the cell is determined by the length, $b$, the width, $a$, and the radius of the fibers, $R^{\#1}$ and $R^{\#2}$. The cell is subjected to a normal load in $x_1-$direction. The boundary conditions are implemented incrementally as follows

$$\begin{aligned} &\dot{T}_2 = 0 \quad \text{and} \quad \dot{u}_1 = 0, \quad \text{on} \quad x_1 = 0 \\ &\dot{T}_1 = 0 \quad \text{and} \quad \dot{u}_2 = 0, \quad \text{on} \quad x_2 = 0 \\ &\dot{T}_2 = 0 \quad \text{and} \quad \dot{u}_1 = \dot{\Delta}_1, \quad \text{on} \quad x_1 = a \\ &\dot{T}_1 = 0, \quad \text{on} \quad x_2 = b \end{aligned} \tag{2}$$

where $\dot{\Delta}_1$ and $\dot{\Delta}_2$ describe incremental displacement quantities on the two edges of the cell, and $T_i$ are surface tractions. The overall macroscopic stress increment, $\dot{\Sigma}_{ij}$, are computed as

$$\begin{aligned} \dot{\Sigma}_{11} &= \frac{1}{tb}\int_0^b \dot{T}_1 t dx_2, \qquad \text{at} \quad x_1 = a \\ \dot{\Sigma}_{22} &= \frac{1}{ta}\int_0^a \dot{T}_2 t dx_1, \qquad \text{at} \quad x_2 = b \end{aligned} \tag{3}$$

and the corresponding macroscopic incremental strains are defined as

$$\dot{E}_{11} = \frac{\dot{\Delta}_1}{a}, \quad \dot{E}_{22} = \frac{\dot{\Delta}_2}{b} \tag{4}$$

Assuming $\Sigma_{33} = 0$, the composite is assumed to deform by uniaxial normal loading under plane stress condition. It means, the modeling simulates the specimen surface at which the debonding is monitored by the SEM. In Fig. 3c, the schematic drawing of the specimen with the debonded interfaces are shown after applying tensile load. In each fiber two parameters are measured; The crack opening distance of the inner and outer interface of the fibers which are denoted by $\Delta_{Inn}$ and $\Delta_{Out}$, respectively and also the debonding angle being called here as the debonding angle. As shown in Fig. 3c, two angles have been measured in each fiber with debonded interfaces. The crack angle at the inner interface of the fiber #1 is denoted with $\theta^{\#1}_{Inn}$ and the crack angle at the outer interface of the fiber #1 is shown with $\theta^{\#1}_{Out}$. The same notation is used for fiber #2.

### 3.1 Isotropic Plasticity Model

The matrix is assumed to be an elasto-plastic material governed by the standard $J_2$-plasticity theory, while the fibers are considered as purely elastic. Both the matrix as well as the fibers are modelled as isotropic materials. In the matrix, the stress increment is calculated from the total strain increment, $\dot{\epsilon}_{ij}$, which consists of an elastic part, $\dot{\epsilon}^e_{ij}$, and a plastic part, $\dot{\epsilon}^p_{ij}$

$$\begin{aligned} \dot{\epsilon}_{ij} &= \dot{\epsilon}^e_{ij} + \dot{\epsilon}^p_{ij} \\ \dot{\sigma}_{ij} &= L_{ijkl}\dot{\epsilon}_{kl} \end{aligned} \tag{5}$$

Here, $L_{ijkl}$ is the fourth order incremental stiffness tensor defined as

$$L_{ijkl} = \frac{E_m}{1+\nu_m}[\frac{1}{2}\left(\delta_{ik}\delta_{jl}+\delta_{il}\delta_{jk}\right) + \frac{\nu_m}{1-2\nu_m}\delta_{ij}\delta_{kl} - \beta\frac{3}{2}\frac{\frac{E_m}{E_t}-1}{\frac{E_m}{E_t}-\frac{(1-2\nu_m)}{3}}\frac{s_{ij}s_{kl}}{\sigma_e^2}] \tag{6}$$

while,

$$\beta = \begin{cases} 1 & \text{for } \sigma_e = \sigma_f \text{ and } \quad \dot{\sigma}_e \geq 0 \\ 0 & \text{for } \sigma_e < \sigma_f \text{ or } \quad \dot{\sigma}_e < 0 \end{cases} \tag{7}$$

where, $E_m$ is the Young's modulus and $\nu_m$ is the Poisson's ratio of the matrix. The tangential modulus, $E_t$, is the slope of the stress-strain curve at the stress level $\sigma_e = \sqrt{\frac{3}{2}s_{ij}s_{ij}}$ and $\delta_{ij}$ denotes the Kronecker delta. The stress deviator is defined by $s_{ij} = \sigma_{ij} - \delta_{ij}\frac{\sigma_{kk}}{3}$. In Eq. 7, $\dot{\sigma}_e = \frac{3s_{kl}\dot{\sigma}_{kl}}{2\sigma_e}$ and $\sigma_f$ is the instantaneous flow stress. During plastic yielding $\beta$ is unity and the magnitude of $L_{ijkl}$ depends on the stress state and the deformation hardening law whereas in the elastic regime (including elastic unloading) it is governed by Hooke's law where $\beta$ is zero. The yield surface, $f$, is taken as the von Mises yield surface

$$f = \sigma_e - \sigma_f(\epsilon^p_e) = 0 \tag{8}$$

Here, $\sigma_f = \sigma_f(\epsilon^p_e)$, where and $\epsilon^p_e$ is the equivalent plastic strain, work conjugate to $\sigma_e$, and it is defined incrementally by the relation $\dot{\epsilon}^p_e = \sqrt{\frac{2}{3}\dot{\epsilon}^p_{ij}\dot{\epsilon}^p_{ij}}$. The hardening behavior determined by the uniaxial stress-strain relation which is represented by the power hardening law

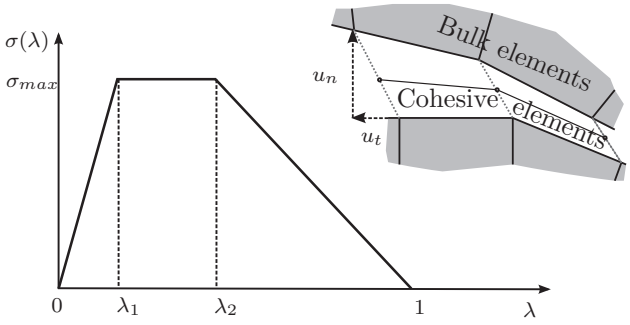


Figure 4: Traction-separation law used to characterize interface separation.

$$\epsilon = \begin{cases} \frac{\sigma}{E} & \text{for } \sigma \leq \sigma_y \\ \frac{\sigma_y}{E}\left(\frac{\sigma}{\sigma_y}\right)^n & \text{for } \sigma > \sigma_y \end{cases} \tag{9}$$

where $n$ is the strain-hardening exponent and $\sigma_y$ denotes the initial yield stress.

### 3.2 Cohesive Zone Model

When the cell is deformed, the interfaces between fibers and matrix tend to separate normally as well as tangentially. In order to capture this fracture behavior, a trapezoidal cohesive zone model proposed by Tvergaard and Hutchinson [14] is used (see Fig. 4). As illustrated in Fig. 3c the failure by debonding is taken into account by considering two generally uneven cohesive zones along the two reinforcement interfaces. The cohesive zone model determines the failure behavior imposing a relation between tractions and separations. This traction-separation law is regarded as a phenomenological characterization of the separation zone along the interfaces and not the description of atomic separation, see [14]. In this model, $\lambda$ is defined as a non-dimensional parameter describing the separation as

$$\lambda = \sqrt{\left(\frac{u_n}{\delta^c_n}\right)^2 + \left(\frac{u_t}{\delta^c_t}\right)^2} \tag{10}$$

such that onset of degradation in the cohesive zone starts at a specified value, $\lambda = \lambda_2$, and fully damage occurs when $\lambda = 1$. Here, $\delta^c_n$ and $\delta^c_t$ are the normal and tangential characteristic cohesive lengths, respectively, and $u_n$ and $u_t$ are the normal and tangential separation of the interface,

respectively. A traction potential can be defined as

$$\Phi(u_n, u_t) = \delta_n^c \int_0^\lambda \sigma(\acute{\lambda}) d\acute{\lambda} \qquad (11)$$

from which the normal, $T_n$, and tangential, $T_t$, tractions acting on the interfaces can be devided according to

$$T_n = \frac{\partial \Phi}{\partial u_n} = \frac{\sigma(\lambda)}{\lambda} \frac{u_n}{\delta_n^c}, \quad T_t = \frac{\partial \Phi}{\partial u_t} = \frac{\sigma(\lambda)}{\lambda} \frac{\delta_n^c}{\delta_t^c} \frac{u_t}{\delta_t^c} \qquad (12)$$

The incremental traction vector is related to the displacement increments across the interface as

$$\begin{bmatrix} \dot{T}_t \\ \\ \dot{T}_n \end{bmatrix} = \begin{bmatrix} \frac{\partial T_t}{\partial u_t} & \frac{\partial T_t}{\partial u_n} \\ \\ \frac{\partial T_n}{\partial u_t} & \frac{\partial T_n}{\partial u_n} \end{bmatrix} \begin{bmatrix} \dot{u}_t \\ \\ \dot{u}_n \end{bmatrix} \qquad (13)$$

where the matrix on the right hand side is the cohesive tangent matrix. In pure normal separation ($u_t = 0$) the maximum traction is $T_n = \sigma(\lambda)$ where $\lambda = \frac{u_n}{\delta_n^c}$, while under pure tangential separation ($u_n = 0$) the maximum traction is $T_t = \frac{\delta_n^c}{\delta_t^c}\sigma(\lambda)$ where $\lambda = \frac{u_t}{\delta_t^c}$. Thus, for both the interfaces considered here, five interface parameters need to be specified, i.e. $\delta_n^c$, $\delta_t^c$, $\lambda_1$, $\lambda_2$ and $\sigma_{max}$. In addition, a plateau in the maximum traction level in the trapezoidal cohesive zone model simutaneously allows more Gauss points of cohesive elements to be at the maximum stress. This may lead to more stable numerical solutions in comparison with bilinear and exponential models [1]. However, Tvergaard and Hutchinson [14] discussed that under small scale yielding and small scale fracture process zone the shape of the separation law has a secondary importance and the most critical parameters are the maximum cohesive stress and the characteristic cohesive length. Finally, it should emphesized that this model takes the same fracture energy for all mode mixities although the tangential cohesive length, $\delta_t^c$, is considered to be larger than the normal cohesive length, $\delta_n^c$.

### 3.3 Numerical Methods

For the numerical implementation the incremental form of the principle of virtual work is adopted. Disregarding body forces, the principle reads

$$\int_V \dot{\sigma}_{ij} \delta \dot{\epsilon}_{ij} dV + \int_{S_I} (\dot{T}_n \delta \dot{u}_n + \dot{T}_t \delta \dot{u}_t) dS = \int_S \dot{T}_i \delta \dot{u}_i dS \qquad (14)$$

where $V$ denotes the volume of the unit cell having the surface $S$ and $S_I$ is the surface of the fiber-matrix interface. In Fig. 5 an example of finite element mesh is shown. The mesh consists of 4420 elements including 286 cohesive elements. Eight-node quadrilateral elements with nine Gauss points are used for the bulk materials while six-node quadrilateral elements with three Gauss points are considered for the cohesive zones. As shown in Fig. 5, the mesh is refined near the interfaces. Tvergaard and Legarth [15] characterized the length of the fracture process region, $\ell$, in the cohesive zone during crack growth by the distance from the crack-tip, where $\lambda = 1$, to the point ahead of the crack-tip where $\lambda = \lambda_1$. They found a good resolution and very little mesh dependence when the value of $\ell$ is several times the length, $\Delta_0$, of a square element in the uniform mesh region (here, around the interfaces in Fig. 5). This requirement is satisfied in the present computations as $\ell \geq 10\Delta_0$ corresponding to 10 elements in the active cohesive zone. In each incremental step, $\Delta t$, for

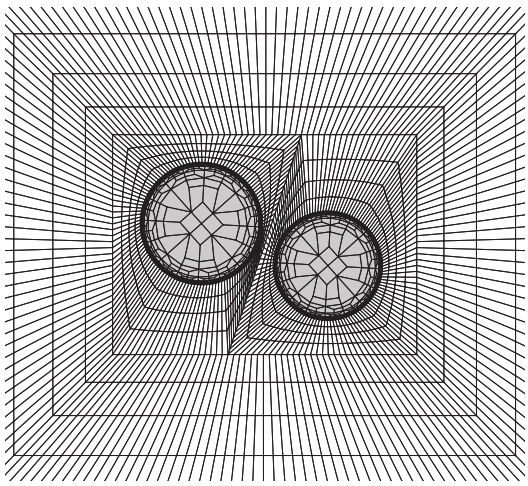

Figure 5: An example of mesh used for the computations. The fiber are positioned in the matrix with the distance of $\Delta_x = 60\mu m$ and $\Delta_y = 20\mu m$ from each other. The fibers radiuses are $R^{\#1} = 25\mu m$ and $R^{\#2} = 28\mu m$.

the next increment is corrected according to $(\dot{\epsilon}^p)_{max} \cdot \Delta t \leq c_1$ and $\left(\dot{\lambda}\right)_{max} \cdot \Delta t \leq c_2$, where the label $max$ refers to the maximum effective plastic strain rate in any Gauss point, or the maximum rate of debonding separation measure at the current increment. Since a forward Euler integration scheme is adopted, it has been investigated if the results are affected by $c_1$ and $c_2$. Thus, the values of the constants $c_1$ and $c_2$ are in several computations chosen as $c_1 = 0.01$ and $c_2 = 0.004$. In addition, discontinuous increment analysis is used, such that when the first Gauss point in the bulk material reaches the plastic regime or when the first Gauss point in the cohesive elements of each interface reaches $\lambda = \lambda_2$ the solver turns one step back and continue the solution with reduced increment size. The amount of step reduction as well as $c_1$ and $c_2$ parameters are chosen such that a stable and converged solution is achieved. Thus, for further reduced time steps similar results are obtained.

## 4. Results and discussion

The in situ observations from the tensile tests conducted inside SEM reveal that debonding at the fiber/matrix interfaces is the first failure mechanism occurring in the two-fiber composite tested here. The results show that the crack initiates at 0° and 180° with respect to the tensile load orientation at $\sim 7MPa$. The applied remote stress is defined by $\sigma_{exp} = \dfrac{F}{A}$ where $F$ and $A$ are the applied tensile load and the area under the load, respectively. Subsequently, the crack propagates at the fiber/matrix interface until a point at which further load leads to crack kinking into the matrix. The applied remote stress at kinking has been measured to be $\sigma_{exp} \sim 14MPa$. In addition, as shown in Fig. 1 the orientation of crack propagating into the matrix is perpendicular to the load orientation indicating mode-I fracture in the matrix. In order to characterize the cohesive parameters used in the numerical modeling, a parameter study has been carried out by fitting the numerical results with the experimental findings. Beside the amount of remote stress at which debonding initiates, the angle of the propagating crack as well as the amount of crack normal opening distance at the

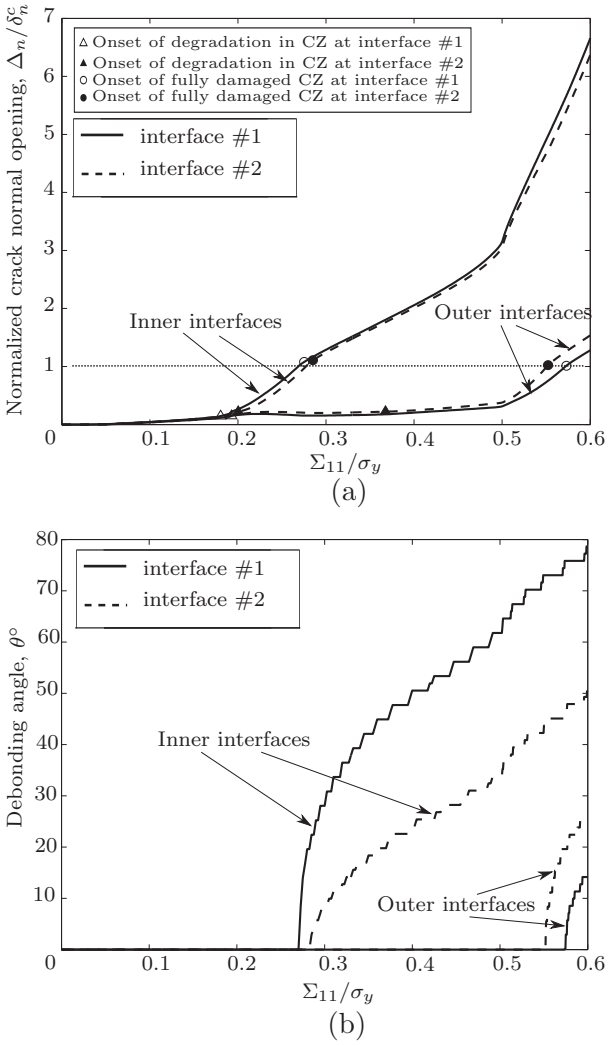


Figure 6: a) The normalized crack normal opening-remote stress and b) the debonding angle-remote stress for the reference case, $R^{\#1} = R^{\#2} = 25\mu m$, $\delta_n^c = 0.006R^{\#1}$, $\delta_t^c = 5\delta_n^c$, $\sigma_{max}^{\#1} = \sigma_{max}^{\#2} = 0.5\sigma_y$, $\lambda_1 = 10^{-4}$, $\lambda_2^{\#1} = 0.1$ and $\lambda_2^{\#2} = 0.2$. The figure illustrates the onset of degradation in the cohesive zone and fully damaged cohesive zone of the two interfaces on the curve.

fiber/matrix interfaces have been measured. This comparison indicates that the maximum cohesive stress is $\sigma_{max} \simeq 8MPa$ and the characteristic cohesive length is $\delta_n^c \lesssim 0.15\mu m$. Calculating the interface normal fracture energy, $\phi$, by $\phi = \dfrac{\sigma_{max}(1 + \lambda_2 - \lambda_1)\delta_n^c}{2}$, the above characterization denotes that the interface normal fracture energy is relative small ($\lesssim 0.5\dfrac{J}{m^2}$) in comparison with the epoxy fracture energy which is normally above $100\dfrac{J}{m^2}$. Furthermore, the very small char-

acteristic cohesive length indicates that failure of glass-fiber/epoxy interfaces are very brittle.

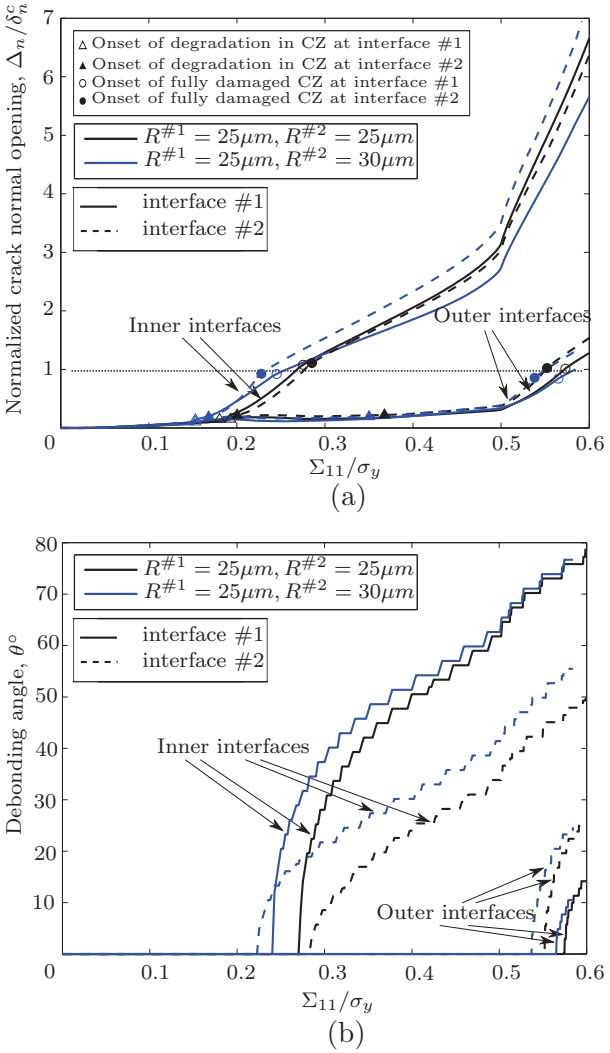


Figure 7: Effect of the fiber radius, $R$, on a) the normalized crack normal opening, $\Delta_n/\delta_n^c$, and b) the debonding angle, $\theta$. The interfaces parameters, the geometry (except the radius of fibers) and loading conditions are identical to the reference case, see Fig. 6.

Using the above characterized cohesive parameters, a parameter study is carried out to assess the effect of fiber positioning and the maximum cohesive stress on the damage evolution of two-fiber composite. In Fig. 6, the behavior of the two-fiber cell for a reference case is shown. The reference case denotes when $R^{\#1} = R^{\#2} = 25\mu m$ and the interfacial parameters for both interfaces are $\delta_n^c = 0.006R^{\#1}$, $\delta_t^c = 5\delta_n^c$, $\sigma_{max}^{\#1} = \sigma_{max}^{\#2} = 0.5\sigma_y$ and $\lambda_1 = 10^{-4}$, while interface #1 has $\lambda_2^{\#1} = 0.1$, and for interface #2, $\lambda_2^{\#2} = 0.2$. Different $\lambda_2$ values which also yield slightly different fracture energies (i.e. $\phi^{\#1} = 0.48\frac{J}{m^2}$ and $\phi^{\#2} = 0.54\frac{J}{m^2}$) lead to uneven interfacial strengths at the two interfaces. Many experiments (e.g. [9] [12]) have shown that the the interfacial fracture energy increases with mode mixity. However, in the current study a cohesive law with the same fracture energy for all mode mixities is used. Fig. 6a and Fig. 6b illustrates the normalized crack normal opening, $\Delta_n/\delta_n^c$, and the debonding angle, $\theta$, respectively. The inner interfaces denote

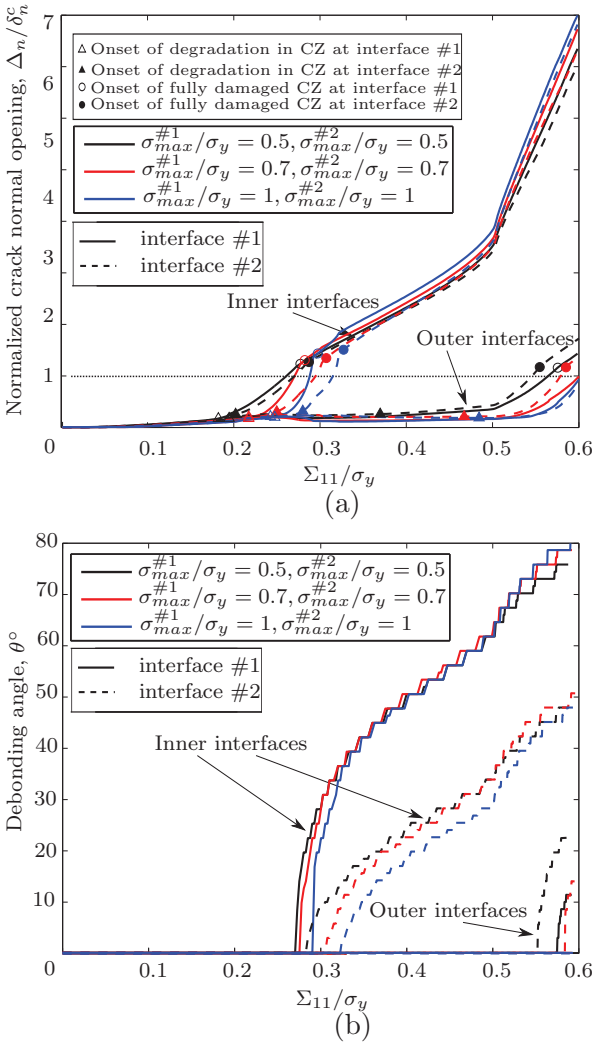


Figure 8: Effect of the maximum cohesive stress, $\sigma_{max}$, on a) the normalized crack normal opening distance, $\Delta_n/\delta_n^c$, and b) the debonding angle, $\theta$. The interfaces parameters (except the maximum cohesive stresses), the geometry and loading conditions are identical to the reference case, see Fig. 6.

the interfaces in the ligament between the two fibers while the outer interfaces are those at the outer side of the fiber far away from the other fiber (see Fig. 2). As shown in Fig. 6a, the initial crack opening occurs at $\frac{\Sigma_{11}}{\sigma_y} \simeq 0.27$ at the inner interfaces and $\frac{\Sigma_{11}}{\sigma_y} \simeq 0.57$ at the outer interfaces which shows that debonding at the interfaces close to the ligaments initiates earlier than those on the outer sides. This clearly shows that the presence of the second fiber strongly affect the debonding of the first fiber. These numerical values of stress at the crack initiation match to the experimental findings reported in the beginning of the result section. At the inner interfaces, by increasing the loading the normalized crack normal opening, $\Delta_n/\delta_n^c$, grows up slightly with a linear slope until the point where debonding leads to nonlinear behavior on the curve. This nonlinearity is due to the degradation of traction-separation in the cohesive low when $\lambda = \lambda_2$ at each cohesive Gauss points. The first Gauss point which reaches $\lambda = \lambda_2$ is depicted by ($\triangle$). Afterwards, subsequent Gauss points at the same cohesive interface also pass $\lambda = \lambda_2$ and therefore the interface gets weaker which leads to nonlinearity on the curve until the first Gauss point at $\Sigma_{11} \simeq 0.28\sigma_y$ gets fully damaged, i.e. $\lambda^{\#1} = 1$, ($\bigcirc$). By continuing loading the crack propagates along interface #1. When interface #1 is being debonded, the normalized crack normal opening versus normalized remote stress shows again a linear behavior until interface #2 starts debonding at $\Sigma_{11} \simeq 0.55\sigma_y$. As for interface #1, the same points are marked but with the filled symbols ($\blacktriangle$ and $\bullet$). The slope of the curves in Fig. 6b represents the crack growth rates. For all cases in the beginning of the crack growth the slope is very sharp denoting that the crack propagates very fast and unstable. But subsequently the slope decreases and the crack propagates at almost a constant growth rate. París et al. ([10] and [9]) studied the mechanisms of failure in a single fiber surrounded by the matrix under transverse tension. Their observation shows that a crack starts running at the interfaces and after a certain angle (between 60° to 70°) the crack kinks into the matrix. The same interval of kinking angle is confirmed in the present experimental obsevations. However, this research focuses on the failure mechanisms before kinking occurs. Therefore, in Fig. 6b, the curves are shown until maximum $\theta = 80°$.

Fig. 7 shows the effect of fiber radius size on the crack initiation at the interfaces. In this figure, fiber #1 has $R^{\#1} = 25\mu m$ while the radius of fiber #2 is $R^{\#2} = 30\mu m$. As depicted in Fig. 7a (see $\bigcirc$-marks and $\bullet$-marks) and in Fig. 7b earlier debonding occurs at the both interfaces when the radius of fiber #2 increases. This earlier debonding can be due to the decrease of the ligament between the two fibers. However, the behavior of the curves remain almost unchanged.

The effect of the maximum cohesive stress is shown in Fig. 8. As illustrated in Fig. 8b, increase of the maximum cohesive stress postpones debonding. But as shown in Fig. 8a, increasing the maximum cohesive stress leads to larger normal crack opening. In addition, Fig. 8b depictes that the cracks of the inner interfaces after $\sim 40°$ grow exactly on the same curve regardless of the maximum cohesive changes.

Lastly, Fig. 9 illustrates the corresponding contours of the accumulated equivalent plastic strain, $\epsilon_e^p$, for the reference case when the remote stress in $x_1$-direction is $\frac{\Sigma_{11}}{\sigma_y} = 0.6$ (see Fig. 6). Some plastic deformation can be seen in the ligament between two fibers but most plastic deformations are in front of the crack tips in the top and bottom of the fibers. This plasticity in the vicinity of the crack tips is due to the tensile stress in $x_1$-direction which eventually leads to shear debonding at the interfaces in the top and bottom of the fibers. Fig. 9 also shows the same crack normal opening in the inner interfaces as well as at the outer interfaces. Although the outer interfaces have smaller crack openings than the inner interfaces. In addition, the debonding at the inner interface in the ligament between the fibers, $\theta_{Inn}^{\#2} = 51°$, shows smaller crack angle than the inner interface away from the ligament, $\theta_{Inn}^{\#1} = 79°$.

## 5. Conclusion

The interfacial parameters are characterized by comparing the experimental results with those from the finite element analysis using the cohe-

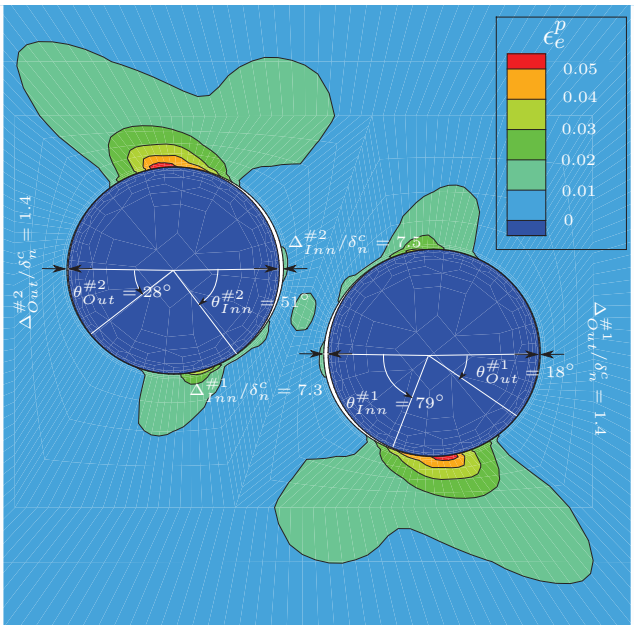


Figure 9: Contours of the accumulated equivalent plastic strain, $\epsilon_e^p$, at $\Sigma_{11}/\sigma_y = 0.6$, see Fig. 6.

sive zone model. The experimental results are determined by performing the in situ tensile tests on a two-fiber composite inside the chamber of SEM. The characterization shows that the maximum cohesive stress is $\sigma_{max} \simeq 8MPa$ while the characteristic cohesive length is $\delta_n^c \lesssim 0.15\mu m$. These two parameters result that the interface normal fracture energy, $\phi$, to be $(\lesssim 0.5\frac{J}{m^2})$. Then, knowing the actual interface properties, different positioning of fibers is studied to investigate the progressive interfacial damage evolution by focusing on the interaction between two fibers with uneven interfacial strengths. It was found that the interfacial normal fracture energy is significantly small compared to the epoxy fracture energy. The results show that debonding initiates at the inner interfaces followed by the outer interfaces. In addition, debonding triggers earlier if the radius of one of the fibers increases. Finally, larger maximum cohesive stress leads to stronger interfaces and subsequently postpones debonding of the interfaces.

**Acknowledgement**

The authors would like to thank the research technicians: Steen J. Bang, Christian H. Madsen and Jonas Heininge for their assistance with specimen preparation. This work is supported by the Danish Council for Strategic Research (grant no.:09-067212) under the Danish Center for Composite Structures and Materials for Wind Turbines.

## References

[1] N. Chandra, H. Li, C. Shet, H. Ghonem "Some issues in the application of cohesive zone models for metal?ceramic interfaces". *International Journal of Solids and Structures*, Vol.39, pp 2827-2855, 2002.

[2] A. Godara, L. Gorbatikh, G. Kalinka, A. Warrier, O. Rochez, L. Mezzo, F. Luizi, A.W. van Vuure, S.V. Lomov, I. Verpoest "Interfacial shear strength of a glass fiber/epoxy bonding in composites modified with carbon nanotubes". *Composites Science and Technology*, Vol.70, pp 1346-1352, 2010.

[3] J.W. Hutchinson and Z. Suo "Mixed Mode Cracking in Layered Materials". *Advances in Applied Mechanics*, Vol.29, pp 63-191, 1992.

[4] J.W. Hutchinson "Mixed mode fracture mechanics of interfaces". *Metal-Ceramics, Acta-Scripta Metallurgica Proceedings Series* Vol.4, pp 295-306, 1990.

[5] A. Kelly, W.R. Tyson "Tensile properties of fiber-reinforced metals: cop- per/tungsten and copper/molybdenum". *Journal of the Mechanics and Physics of Solids* Vol.13, pp 329-350, 1965.

[6] B.K. Larson, L.T. Drzal "Glass fibre sizing/matrix interphase formation in liquid composite moulding: effects on fibre/matrix adhesion and mechanical properties". *Composites* Vol.25, pp711-21, 1994.

[7] B.N. Legarth and C.F. Niordson "Debonding failure and size effects in micro-reinforced composites". *International Journal of Plasticity* Vol.26, pp 149-165, 2010.

[8] J.M. Molina-Aldareguía, M. Rodríguez, C. González, J. LLorca "An experimental and numerical study of the influence of local effects on the application of the fibre push-in test.". *Philosophical Magazine* Vol.91, pp 1293-1307. 2011.

[9] F. París, E. Correa, J. Cañas "Micromechanical view of failure of the matrix in fibrous composite materials". *Composites Science and Technology* Vol.63, pp 1041-1052, 2003.

[10] F. París, E. Correa, J. Cañas, V. Mantič "Kinking of Transversal Interface Cracks Between Fiber and Matrix". *Journal of Applied Mechanics* Vol.74, pp 703-716, 2007.

[11] B.F. Sørensen, A. Horsewell, P. Skov-Hansen "In- situ observation of crack formation Bi-2223 HTS tapes". *Physica C: Superconductivity* Vol.372-376, pp. 1032-1035, 2002.

[12] B.F. Sørensen, T.K. Jacobsen "Characterizing delamination of fibre composites by mixed mode cohesive laws". *Composites Science and Technology* Vol.69, pp. 445-456, 2009.

[13] V. Tvergaard "Effect of thickness inhomogeneities in internally pressurized elastic-plastic spherical shells". *Journal of the Mechanics and Physics of Solids* Vol.24, pp 291-304, 1976

[14] V. Tvergaard, J.W. Hutchinson "The influence of plasticity on mixed mode interface toughness". *Journal of the Mechanics and Physics of Solids* Vol.41, pp 1119-1135, 1993.

[15] V. Tvergaard, B.N. Legarth "Effect of anisotropic plasticity on mixed mode interface crack growth". *Engineering Fracture Mechanics* Vol.74, pp 2603-2614, 2007.

[16] S.F. Zhandarov, E.V. Pisanovab "The local bond strength and its determination by fragmentation and pull-out test". *Composites Science and Technology* Vol.57, pp 957-64, 1997.